Biologia (2022) 77:1373–1389
https://doi.org/10.1007/s11756-022-01012-y

ORIGINAL ARTICLE

In silico studies on structural inhibition of SARS-CoV-2 main protease M^{pro} by major secondary metabolites of Andrographis paniculata and Cinchona officinalis

Moumita Majumdar[1] · Vishal Singh[2] · Tarun Kumar Misra[1] · Dijendra Nath Roy[3,4]

Received: 2 September 2021 / Accepted: 10 January 2022 / Published online: 28 February 2022

Abstract

The COVID-19 infection by Novel Corona Virus (SARS-CoV-2) has become one of the largest pandemic diseases, with cumulative confirmed infections of 275,233,892 and 5,364,996 deaths to date according to World Health Organization. Due to the absence of any approved antiviral drug to treat COVID-19, its lethality is getting severe with time. The main protease of SARS-CoV-2, M^{pro} is considered one of the potential drug targets because of its role in processing proteins translated from viral RNA. In the present study, four of the plant metabolites, 14-deoxy-11,12-didehydroandrographolide, andrograpanin, quinine, cinchonine from two eminent medicinal plants *Andrographis paniculata and Cinchona officinalis*, have been evaluated against the main protease of SARS-CoV-2 through *in-silico* molecular docking and molecular dynamics simulation study. From the result interpretations, it is found that andrograpanin has strong binding affinities with the target protein in its active site with potential negative energies. Molecular Dynamic simulation and MMGBSA studies suggest that earlier reported N3 inhibitor and andrograpanin exhibit effective binding interactions involving identical amino acid residues with the same binding pockets of the main protease of SARS-CoV-2. Therefore, the theoretical experiment suggests that andrograpanin, could be considered the promising inhibitor against SARS-CoV-2 M^{pro}.

Keywords SARS-CoV-2 · M^{pro} · Inhibitors · Plant metabolites · Molecular docking · Molecular dynamic simulation

Abbreviations

WHO	World Health Organization
CoVs	Coronavirus
SARS	severe acute respiratory syndrome
α	Alpha
β	beta
γ	gamma
δ	delta
M^{pro}	Main Protease
IC50	Inhibition Concentration
MD	Molecular dynamics
RMSD	Root Mean Square Deviation Root Mean Suuare Deviation
RMSF	Root Mean Square Fluctuation Root Mean Suuare Deviation
ns	nanosecond
OPLS	optimized potential for liquid simulations
SPC	simple point charge
ps	Recording interval

✉ Dijendra Nath Roy
dnr_20@hotmail.com

[1] Department of Chemistry, National Institute of Technology-Agartala, Agartala, Tripura PIN-799046, India

[2] Department of Applied Sciences, Indian Institute of Information Technology-Allahabad, Devghat, Jhalwa, Allahabad, Uttar Pradesh PIN-211012, India

[3] Department of Bioengineering, National Institute of Technology-Agartala, Agartala, Tripura PIN-799046, India

[4] Department of Botechnology, National Institute of Technology-Raipur, Raipur, Chhattisgarh PIN-492010, India

Introduction

Since the beginning of 2020, the coronavirus disease or COVID-19 caused by SARS CoV 2 has evolved to be one of the most threatening pandemics; to date, it has caused more than 275,233,892 infections among people with 5,364,996 deaths around the world, according to World

Health Organization (WHO) (https://www.who.int/emergencies/diseases/novel-coronavirus-2019) reports. The whole family of coronavirus is named based on their structures, i.e., 'Corona' means the crown (Crown, Latin – Corona), which has crown-like spikes on the surface. The Scientists June Almeida and David Tyrrell, who first observed this virus under the microscope during their study, coined the term 'Coronavirus' (Sturman and Holmes 1983). SARS-CoV-2 can infect a wide range of hosts that include animals, humans. The infection symptoms in humans include common cold, mild to severe respiratory illness. One of the most significant consequences of COVID-19 is secondary bacterial and/or fungal infection, which are crucial for mortality. But to date, this issue has not been explored much with serious attention (Zhou et al. 2020a, b). The transmission of coronavirus is as common as other respiratory viruses, which is through larger droplets at the time of cough and sneeze (https://www.who.int/health-topics/coronavirus#tab=tab1). These can propagate actively up to five to six feet approximately in surrounding from the infected individuals (McIntosh et al. 2021). Coronavirus mediates infection through the host immune system. One research group has demonstrated that coronavirus (CoVs) can initiate pathogenesis by obstructing the innate immune system (Lei et al. 2018). Apart from that, surface contact with the infected ones can cause viral transmission. The very first corona outbreak in humans was reported in 2002 caused by severe acute respiratory syndrome coronavirus (SARS-CoV) (Organization 2003). The recent pandemic coronavirus is called severe acute respiratory syndrome coronavirus2 (SARS-CoV-2) because its structure highly resembles SARS-CoV (Zheng 2020).

CoVs are single-stranded RNA viruses, circular with a diameter of 65–125 nm. The genetic material, RNA, is 26 to 32kbs in length, known to be the largest viral genome (Sahin et al. 2019). The viruses have subgroups like Alpha (α), beta (β), gamma (γ), and delta (δ) coronavirus. Different types of proteins encapsulate the viral genetic material, and the most predominant feature of CoVs is these proteins, which are of different types, namely spike (S) proteins appeared crown-like structure, membrane (M) protein, envelope (E) protein, and nucleocapsid (N) proteins (Fehr and Perlman 2015). These protein shells made up of these proteins provide a hard protective layer for genetic material at the time of viral transmission and pathogenesis. Spike proteins on the outer layer allow the virus to infect the host by integration with the cell membrane receptor proteins. Unlike other respiratory viral infections, SARS-CoV-2 does not need to enter the host cell nucleus for replication. It can act as an integral part of the host cell by regulating the host cellular ribosomes to make viral proteins (Astuti 2020). All the packaging structures travel through vesicles and assemble just beneath the cell membrane, and bud off from the cell as a virion. CoVs get matured through an incredibly multifaceted polyprotein cascade achieved by proteolytic processing of two proteins, namely pp1a and pp1ab (Xue et al. 2008; Zhou et al. 2020a, b). This further controls replication and expression of viral genes. CoV main protease (CoV M^{pro}), known as 3CL protease or $3CL^{pro}$, arbitrates the maturation cleavage of pp1a and pp1ab precursor polyprotein at 11 cleavage sites (Xue et al. 2008). CoV M^{pro} is considered a prime target for the development of antiviral compounds against SARS-CoV-2 because it plays a significant role in self-maturation and sequential replicase polyprotein maturation (Xia and Kang 2011).

Natural products are usually in practice for the novel medication in therapeutic research and strategy, which has been followed since ancient times due to its promising potency to treat various human diseases Cragg and Newman 2013; Majumdar et al. 2019; Majumdar et al. 2020c; Majumdar et al. 2020d; Majumdar et al. 2020e; Roy et al. 2010; Roy et al. 2011). Several terpenoids and phenols, the secondary metabolites of plants like *Andrographis paniculata*, and *Cinchona officinalis* showed immense biomedical applications, including anti-malarial, anti-bacterial, anti-fungal, anti-cancerous, anti-inflammatory, as well as antiviral activities (Chen et al. 2009; Li et al. 2006; Majumdar et al. 2020b; Majumdar and Roy 2019; Roy et al. 2010, 2011; Talactac et al. 2015). These plant products proved to be nontoxic for the animal in comparison to the synthetic drugs. Thus biomolecules extracted from medicinal plants may be utilized as novel therapeutic molecules because there is no successful medication reported against SARS-CoV-2.

In the present study, the main protease of SARS-CoV and SARS-CoV-2 is well-chosen as a prime target to predict the possible interactions with some of the plant metabolites, like 14-deoxy-11,12-didehydroandrographolide, andrograpanin, quinine, cinchonine, acting as inhibitors through *in silico* studies. Accordingly, the present study shows the potential interaction between four natural compounds of interest, 14-deoxy-11,12-didehydroandrographolide, andrograpanin, quinine, and cinchonine with the target proteins M^{pro} having significant binding energies in the active sites. Additionally, MD simulation studies reveal structural stabilities during complex formation, and inhibition concentration (IC50) values indicate these compounds have no lethal effects on therapeutic execution. The exciting findings suggest that these specific plant metabolites may be acted for medication following different phases of trials in the drug development process associated with anti-SARS-CoV-2 therapeutics.

Methods

Docking through Autodock

The ligands are 14-deoxy-11,12-didehydroandrographolide (PubchemID: 5,708,351), Andrograpanin (Pubchem ID: 11,666,871), Quinine (PubchemID:

3,034,034), and Cinchonine (Pubchem ID: 90,454). The target molecules are the viral dimeric proteins, namely M^{pro} of SARS-CoV (PDB ID:2GTB) (Lee et al. 2007) and M^{pro} of SARS-CoV-2 (PDB ID: 6LU7) (Jin et al. 2020), which play a vital role in the absolute processing of viral proteins in the host cells. These ligands and targets were considered for *in-silico* docking studies. AutoDock version 4.2.6 through system setting with ADT 1.5.6 software was used to investigate the molecular simulation studies (Morris et al. 2009).

At the beginning of molecular docking, hetam (ligand) and water molecules were removed from the crystallographic structures. Consequently, following Lamarckian genetic algorithm (LGA) in Autodock, polar hydrogens were added to the proteins, and charges were consigned according to Gasteiger (Gasteiger and Marsili 1980). Besides, a grid map with a spacing of 0.375Å was set up based on each protein's active site residue for docking score calculations (Jin et al. 2020; Lee et al. 2007). To fit in the active sites, the grid map was fixed in the following dimension at $100 \times 82 \times 70$ points for 2GTB, and $66 \times 120 \times 110$ points for 6LU7 with the spacing of 0.375Å. 100 docking runs were performed after considering the target protein as a rigid model and ligand as a flexible model. The rest of the parameters were set to the default with maximum energy evaluations to 2,500,000 (Dubey et al. 2016). Docking positions with 2.0Å RMSD values were clustered for additional analysis. The representative conformations of the best-docked pose were selected for reporting of each compound.

Docking through Glide

The structure making for Glide was done using the Protein Preparation Wizard of Maestro graphical user interface (Schrodinger LLC, New York). Ionization and tautomeric states were generated accompanied by the addition of Hydrogens by Epik (Shelley et al. 2007), and PROPKA was employed for the orientation setting of proteins (Olsson et al. 2011). All the ligands have undergone standard precision of post-minimization for optimized docking, and Epik state penalties were added to docking scores. 100 poses were generated for each ligand-protein interaction. Glide Score and Glide Emodel scores were calculated using standard protocols (Dubey et al. 2019). The pose selection was attained based on the Emodel (best pose of the ligand) in Glide, and the best poses were ranked with the help of the Glide Score, where increased negative values signify a stronger binding affinity. All the ligands were downloaded from PubChem and subjected to LigPrep, Glide-v8.3 Schrodinger, LLC, New York, NY, 2019-2 for generation different stable conformational conformations for molecular docking and MD simulation under default condition of LigPrep/Epik (Majumdar et al. 2020a).

Molecular dynamics simulation study

Molecular dynamics simulation studies are a strategic protocol to understand the structural properties and the interactions between protein and ligands at the atomic deviation level. Molecular dynamics (MD) simulation calculates and predicts the conformational stability and integrity of protein-ligand complex in real-time environments. MD simulation was accomplished using the desmond to estimate the stability of the protein-ligand complex. Calculation and prediction of different parameters like protein-ligand root mean square Deviation (RMSD), root mean square fluctuation (RMSF), protein-ligand contact bar graph, Simulation quality analysis, and Simulation event analysis was performed to evaluate the structural stability and conformational change of the protein-ligand complex during the 50 nanosecond (ns) simulation.

Protein preparation and grid generation

The crystal structures of SARS-CoV with inhibitor Aza-Pertide Epoxide (2GTB) and SARS-CoV-2 main protease (M^{pro}) with inhibitor N3 (6LU7) were downloaded from protein data bank (RCSB PDB). Preparation of the proteins was done using default parameters of protein preparation wizard (Glide, Maestro v12.0, Schrodinger, LLC, New York, NY, 2019-2). Grid was generated separately around the binding sites predicted via SiteMap and around the M^{pro} residues engaged in molecular interactions with Aza-peptide Epoxide and N3 inhibitor. An orthorhombic box of X=50, Y=50, Z=50, the inner box of X=20, Y=20, Z=20, and grid center near THR24 and THR25 as X=-19.5 Y=20.46 Z=60.41 for SARS-CoV and Outer box of X=50, Y=50, Z=50, and an inner box of X=20, Y=20, Z=20, and grid center near THR24 and THR25 as X=13.28 Y=21.72 Z=66.06 for SARS-CoV-2 using Glide v8.3, Schrodinger, LLC, New York, NY, 2019-2 was built to cover the entire complex with OPLS_2005 force-field (optimized potential for liquid simulations) and SPC (simple point charge) solvent system. Na+/Cl ions were added to balance and neutralize the system and to mimic and stabilize the real-time and in vitro environment, 0.15 M NaCl was additionally provided during the simulation (Bowers et al. 2006). The systems were minimized by applying 1 kcal/mol Å of convergence threshold with 2000 iterations together with pre-equilibration through ingrained relaxation module built-in Desmond, earlier to the final MD simulation process. Additionally, the complexes were exposed to 300 K

and 1Bar pressure for 50 ns NPT collaborative with a 10 ps recording interval.

Molecular dynamics

MD simulations of the complexes were performed after the system-building of the 2GTB-ligand complexes and 6LU7-ligand complexes were completed. The build system of the best-screened complex was loaded for MD simulation for 50 ns for each protein-ligand. Recording interval (ps), energy, trajectory, NPT (temperature – 300 K, pressure = 1.01325 bar) were set as the default value, and the simulation checkpoint interval was saved 240.06 ps. MD simulation was performed using Desmond, Schrodinger, LLC, New York, NY, 2019-1 (Bowers et al. 2006).

Estimation of binding energy through MM-GBSA

Calculation of different binding affinity like dG bind, dG Bind Coulomb, dG Bind Covalent, dG Bind H-bond, and dG Bind Solv. of the docked complex following the default principal condition were performed using Prime, Glide v8.3, Schrodinger, LLC, New York, NY, 2019-2.

Prediction of ADME/T properties (Absorption, Distribution, Metabolism, Excretion, and Toxicity)

The prediction of chemical properties like molecular weight, dipole moment, SASA, QP LogS QP Log HERG QP caco QP Log BB QPPMDCK CIQP LogS FOSA, FISA, and PISA were calculated using QikProp-V6.

Prediction of half of the inhibition concentration (IC50)

In Autodock, after each LGA run, IC50 values for each docked complex are calculated together with the best docking position based on cluster analysis (Kaur et al. 2010; Rao et al. 2015). IC50 values are predicted in terms of the inhibition constant (Ki) of the system (Wei et al. 2007).

Results

In the present study, molecular docking was performed to predict the possible binding of ligands with main proteases of SARS-CoV and SARS-CoV-2. Two steadfast docking platforms i.e. Autodock and Glide were used to validate the docking outcomes of selected natural products with two selected proteins. Crystal structures of two principle protease enzymes M^{pro} of SARS-CoV (2GTB) and M^{pro} of SARS-CoV-2 (6LU7) were selected as the target proteins. Four natural compounds 14-deoxy-11,12-didehydroandrographolide, andrographolide, quinine, and cinchonine (Fig. 1), were evaluated through molecular docking using two platforms and MD simulations by predicting interactions of two main proteases of SARS-CoV and SARS-Cov-2 in comparison with aza peptide epoxide and N3 inhibitor (Lee et al. 2007; Wei et al. 2007). The non-covalent interactions between four ligands and amino acids of proteins are mainly hydrogen bonds, pi-alkyl, alkyl, carbon-hydrogen, hydrophobic and polar interactions (Figs. 2, 3, 4 and 5), and detailed interactions for binding between 14-deoxy-11,12-didehydroandrographolide, andrographanin, quinine, and cinchonine with proteins are listed in Table 1. A set of comprehensive analyses of the molecular interactions of ligands with proteins is demonstrated in Table 1. The complexes formed between the protease of SARS-CoV and SARS-CoV-2 and four different ligands exhibit stable chemical bonds with active sites of the enzymes (Thr24, Thr26, Leu27, His41, Met49, Ser144, Asn142, Cys145, His163, Gln 189, etc.) reported in the literature (Jin et al., 2020; Lee et al. 2007). A correlation chart of Glide and Autodock scores has been represented in Table 2. Pre and post-simulation analysis reveal compounds 2 and 4 bind in the same cavity where aza peptide epoxide binds with SARS-CoV and compound 2 binds with the identical cavity of N3 by sharing typically matching amino acid residues of target proteins, predicted to be involved in the protein-ligand interaction (Jin et al., 2020; Lee et al. 2007).

M^{pro} of SARS CoV-2 is an unusual cysteine protease accountable for the replication and contamination by

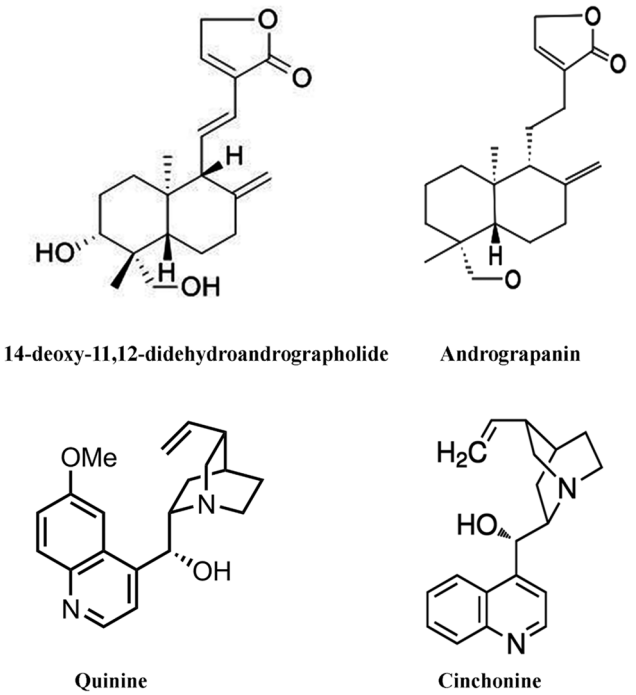

Fig. 1 Chemical structures of 14-deoxy-11,12-didehydroandrographolide, Andrograpanin, Quinine, and Cinchonine

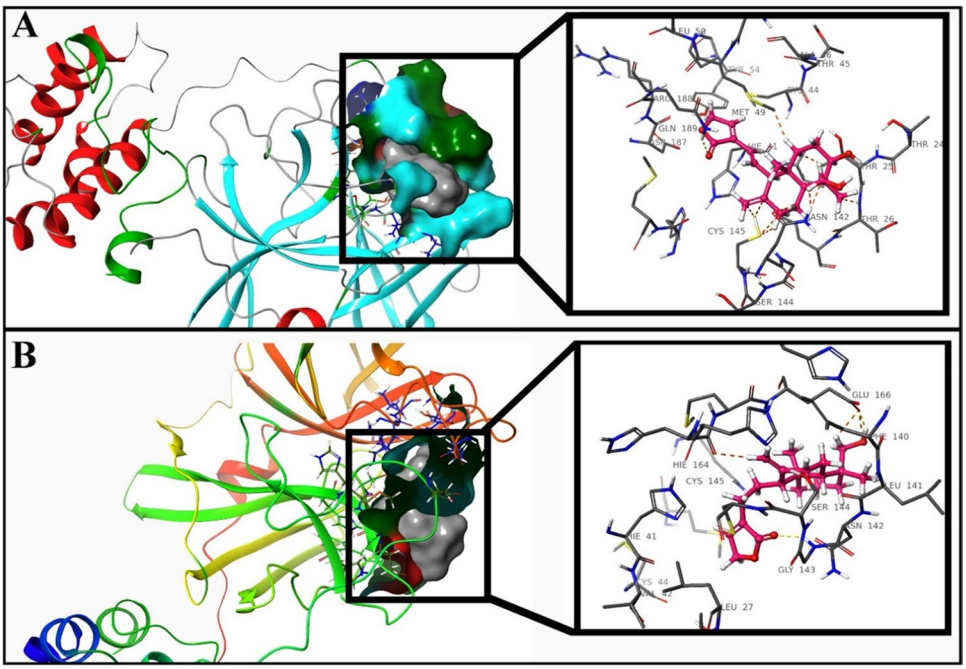

Fig. 2 The interaction map of M^{pro} Protein of SARS-CoV (PDB ID 2GTB) with ligands; (**A**) Docking interaction of 14-deoxy-11, 12 didehydroandrographolide (Pubchem 5708351) with SARS-CoV, (**B**) Docking interaction of Andrograpanin (Pubchem ID 11666871)

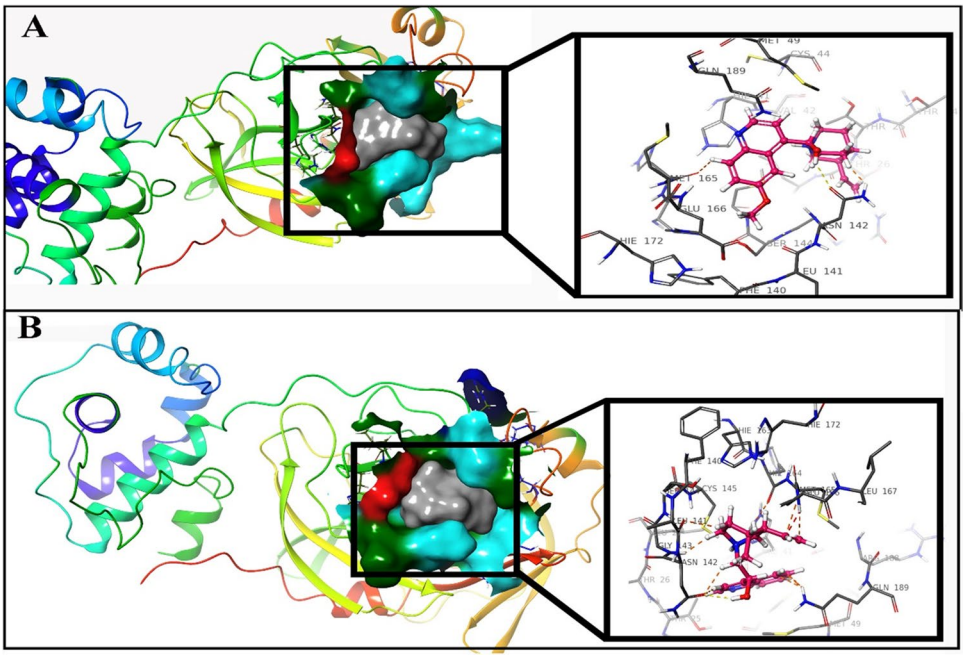

Fig. 3 The interaction map of M^{pro} Protein of SARS-CoV (PDB ID 2GTB) with ligands; (**A**) Docking interaction of Quinine (Pubchem 3034034) with SARS-CoV, (**B**) Docking interaction of Cinchonine (Pubchem ID 90454) with SARS-CoV

the virus (Citarella et al. 2021). Two viral polyproteins precursors, pp1a (486 kDa) and pp1ab (790 kDa), are involved in the intracellular replication of SARS-CoV. These two protein precursors transcribe a replicase enzyme complex which mediates the subsequent downstream reactions (Thiel et al. 2001). There are 11 cleavage sites of CoV M^{pro} in the central and C-terminal regions of the two polyproteins. The cleavages lead to the release of the key protein for viral replication, specifically an RNA polymerase and a helicase (Thiel et al. 2003). The main protease M^{pro} of SARS-CoV-2 has 96% sequence similarity with SARS-CoV (Chen et al. 2020). The enzyme's active site consists of 4 pockets explicitly S1, S2, S3, S4. S1 binding pocket is a catalytic dyad having Cys145 and His41 residues and is interleaved in a cleft amid domains I and II of the protease enzyme (Citarella et al. 2021). Therefore, the drug candidate, which shows attenuation against SARS-CoV M^{pro}, can be substantially effective

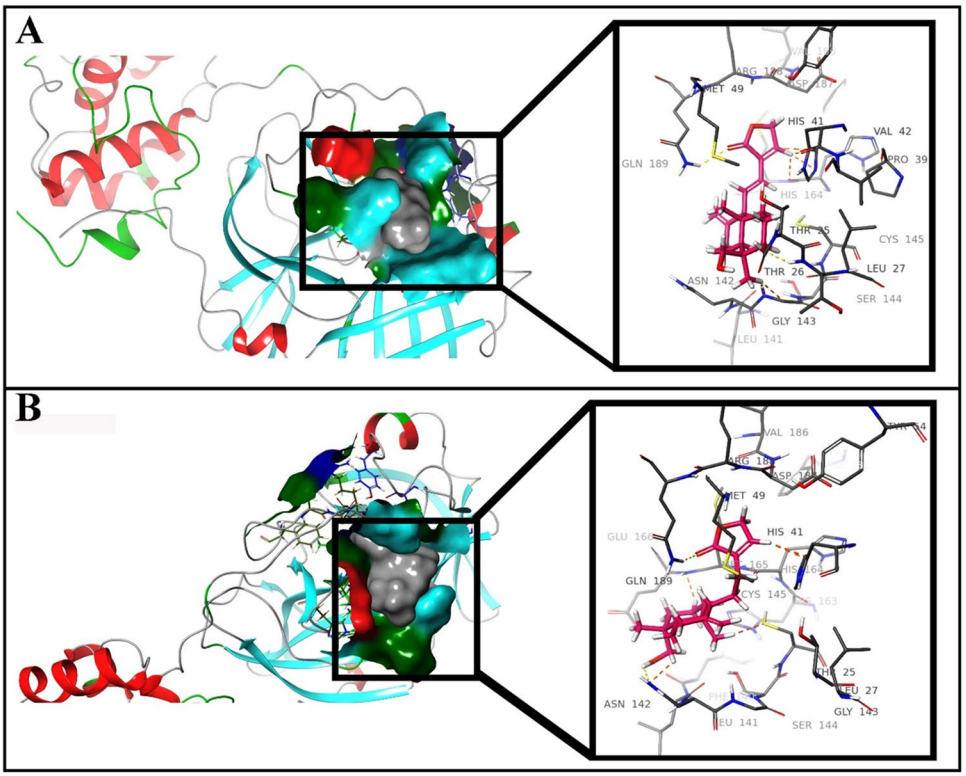

Fig. 4 The interaction map of M^{pro} Protein of SARS-CoV-2 (PDB ID 2GTB) with ligands; (**A**) Docking interaction of11, 12 deoxy-14 didehydroandrographolide (Pubchem 5708351) with SARS-CoV-2, (**B**)Docking interaction of Andrograpanin (Pubchem ID 11666871) with SARS-CoV-2

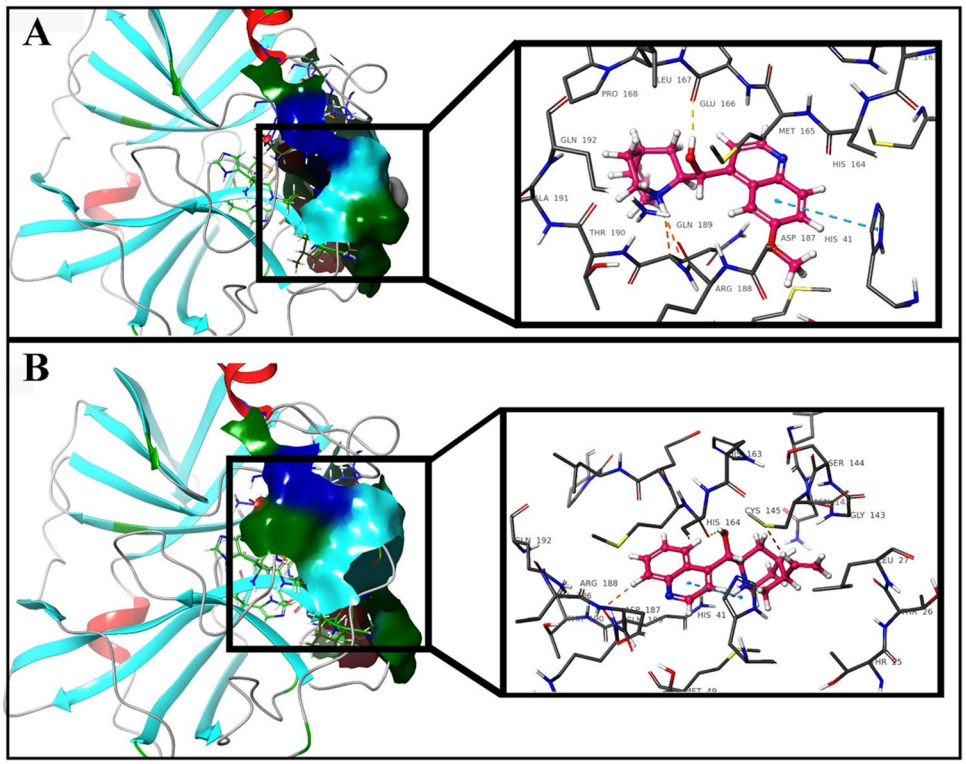

Fig. 5 The interaction map of M^{pro} Protein of SARS-CoV-2 (PDB ID 2GTB) with ligands; (**A**) Docking interaction ofQuinine (Pubchem 3034034) with SARS-CoV-2, (**B**) Docking interaction ofcinchonine (Pubchem ID 90454) with SARS-CoV-2

against the Mpro activity of SARS-CoV-2. The M^{pro} is a cysteine peptidase in nature. The main protease of SARS-CoV-2, also known as M^{pro} has indispensable roles in processing the polyproteins translated directly from the viral RNA (Hilgenfeld 2014) and viral replication and transcription (Jin et al. 2020). In the following sections,

Table 1 Molecular interactions of SARS-CoV M^{pro} and SARS-CoV-2 M^{pro} with natural compounds

Protein (PDB ID)	Compound (PubChem ID)	Autodock Result (Types of Bonds)	Glide Result (Types of Bonds)
M^{pro} (2GTB)	14-deoxy-11,12-didehydroandrographolide (PubChem ID: 5708351)	**His41** (alkyl), **Met49** (sulphur), **Ser144** (hydrogen), Cys145 (alkyl), His163 (hydrogen), His164 (carbon hydrogen), and **Gln189** (carbon hydrogen)	Thr24 (polar), Thr26 (polar), Leu27 (hydrophobic), **His41** (polar), Cys44 (hydrophobic), **Met49** (hydrophobic), Pro52 (hydrophobic), Tyr54 (hydrophobic), Asn142 (Polar), **Ser144** (Polar), Cys145 (hydrophobic), Met165 (hydrophobic), and **Gln189** (hydrogen)
	Andrograpanin (PubChem ID: 11666871)	**His41** (alkyl, pi-alkyl), **Phe140** (carbon hydrogen), **Asn142** (carbon hydrogen), **Cys145** (pi-alkyl bond), **His163** (alkyl), His172 (alkyl), and Gln189 (carbon hydrogen)	Thr24 (polar), **His41** (polar), **Phe140** (hydrophobic), Leu141(hydrophobic), **Asn142** (polar), Gly143 (hydrogen), Ser144 (polar), **Cys145** (hydrophobic) and **His163** (polar), His164 (polar), Met165 (hydrophobic), and Glu166 (hydrogen)
	Quinine (Pubchem ID: 3034034)	**His41** (pi-pi stacking), **Leu141** (alkyl), **Asn142** (carbon hydrogen), Cys145 (hydrogen bond, unfavourable bump), His163 (pi-alkyl), **His164** (hydrogen), and **Met165** (pi-sulphur)	Thr25 (polar), Thr26 (polar), Leu27 (hydrophobic), **His41** (polar), Met49 (hydrophobic), Phe140 (hydrophobic), **Leu141** (hydrophobic), **Asn142** (hydrogen and polar), Ser144 (polar), Cys145 (hydrophobic), His163 (polar), **His164** (polar), and **Met165** (hydrophobic) Gln189 (polar)
	Cinchonine (Pubchem ID: 90454)	**His41** (pi-pi stacking), **Met49** (pi-sulphur), **Asn142** (carbon hydrogen), and **Met165** (pi-sulphur)	Thr24 (polar), **His41** (polar), Cys44 (hydrophobic), **Met49** (hydrophobic), Phe140 (hydrophobic), Leu141 (hydrophobic), **Asn142** (hydrogen and polar), Ser144 (polar), Cys145 (hydrophobic), His163 (polar), His164 (polar), **Met165** (hydrophobic) and Gln189 (polar)
M^{pro} (6LU7)	14-deoxy-11,12-didehydroandrographolide (PubChem ID: 5708351)	**His41** (pi-alkyl), **Met49** (alkyl), Ser144 (hydrogen), Asn142(hydrogen), **Cys145** (pi-alkyl), and **Gln189** (carbon hydrogen)	Thr25 (polar), Thr26 (hydrogen and polar), Leu27 (hydrophobic), **His41** (polar), Val42 (hydrophobic), **Met49** (hydrophobic), Tyr54 (hydrophobic), Asn142 (polar), His164 (polar), Gln189 (polar), Leu141 (hydrophobic), **Cys145** (hydrophobic), Met165 (hydrophobic), and **Gln189** (hydrogen)
	Andrograpanin (PubChem ID: 11666871)	**Asn142** (unfavourable bump), **Cys145** (hydrogen, alkyl), , **His163** (alkyl, pi-alkyl), and Glu166 (hydrogen)	His41 (polar), Met49 (hydrophobic), Thr54 (hydrophobic), Leu141 (hydrophobic), **Asn142** (polar), Ser144 (polar), **Cys145** (hydrophobic), **His163** (polar), His164 (polar), Met165 (hydrophobic) and Gln189 (polar)
	Quinine (Pubchem ID: 3034034)	**His41** (alkyl, pi-alkyl), **Met49** (alkyl, pi-alkyl bond), Leu141 (amide pi-stacking), Ser144 (carbon hydrogen), **Cys145** (hydrogen, pi-sulphur), His163 (carbon hydrogen), His164 (carbon hydrogen), and **Gln189** (carbon hydrogen)	**His41** (polar), Cys44 (hydrophobic), **Met49** (hydrophobic), Pro52 (hydrophobic), Tyr54 (hydrophobic), **Cys145** (hydrophobic), His164 (polar), Met165 (hydrophobic), Leu167 (hydrophobic), Pro168 (hydrophobic), **Gln189** (polar) and Thr190 (polar)
	Cinchonine (Pubchem ID: 90454)	**His41** (pi-pi stacking), Met49 (pi-alkyl), **Asn142** (carbon hydrogen), **Cys145** (hydrogen and alkyl), **His164** (hydrogen), and **Met165** (pi-alkyl)	Thr25 (polar), Thr26 (polar), Leu27 (hydrophobic), **His41** (polar and Pi-Pi Stacking), Met49 (hydrophobic), Tyr54 (hydrophobic), **Asn142** (polar), Ser144 (polar), **Cys145** (hydrophobic), His163 (polar), **His164** (hydrophobic and polar), **Met165** (hydrophobic), Gln189 (polar) and Thr190 (polar)

* Bold fonts indicate the common interactions predicted in AutoDock and Glide software

Table 2 Molecular docking simulation of SARS-CoV M^{pro} and SARS-CoV-2 M^{pro} with natural compounds through best predicted binding energies

Protein (PDB ID)	Compound (PubChem ID)	Dock score (kcal/mole)	Glide score (kcal/mole)	Glide e-model (kcal/mole)
M^{pro} (2GTB)	14-deoxy-11,12-didehydroandrographolide (PubChem ID: 5,708,351)	-6.96	-5.653	-41.242
	Andrograpanin (PubChem ID: 11,666,871)	-7.02	-5.093	-39.197
	Quinine (Pubchem ID: 3,034,034)	-6.19	-5.002	-43.022
	Cinchonine (Pubchem ID: 90,454)	-5.516	-5.532	-44.811
M^{pro} (6LU7)	14-deoxy-11,12-didehydroandrographolide (PubChem ID: 5,708,351)	-5.83	-4.529	-35.918
	Andrograpanin (PubChem ID: 11,666,871)	-4.97	-5.929	-42.365
	Quinine (Pubchem ID: 3,034,034)	-4.77	-5.459	-41.711
	Cinchonine (Pubchem ID: 90,454)	-4.81	-5.585	-44.396

we will demonstrate that there are mainly non-covalent interactions between the substrate-binding pockets of M^{pro} (Jin et al. 2020) and the compounds of interest (14-deoxy-11,12-didehydroandrographolide, andrograpanin, quinine, and cinchonine), resulting in inhibition of the viral proteins and their functions.

Interaction between M^{pro} (2GTB) of SARS-CoV and natural compounds

The complexs obtained from Autodock and Glide illustrates formation of hydrogen bond (H bond), alkyl bond, cabcon hydrogen bond take place in between 14-deoxy-11,12-didehydroandrographolide and Ser144(bond length 3.068 Å), of M^{pro} (Table 1), along with active site residue Gln189 (bond length 1.81 Å), His41, Cys44, Met49, by means of-5.653 kcal/mole energy (Fig. 2A, Table 1).

Andrograpanin forms the non-covalent bonds with His 41, Phe140, Asn142, Cys145, and His163 with -5.093 kcal/mole energy. Interestingly Gly143 (bond length 2.48 Å) and Glu166 (bond length 3.07 Å) of peotein form H bond with the ligand (Fig. 2B; Table 1).

Quinine interacts with M^{pro} enzyme through conventional hydrogen bond formation at Asn142 (bond length 2.34 Å) and His164 (bond length 2.965 Å) with -5.002 kcal/mole glide score. There are carbon-hydrogen bond, and the pi-alkyl bond between the ligand and Leu141 and Met 165 of M^{pro} (Fig. 3A, Table 1).

The protein-ligand complex of cinchonine with SARS-CoV exhibits non-covalent interactions, including pi-pi stacking, pi-sulfur bond, and carbon-hydrogen bond with His41, Met49, Asn142 (H bond length 2.459 Å) and Met165 through of glide score -5.50 kcal/mole (Fig. 3B; Table 1).

Interaction between M^{pro} (6LU7) of SARS-CoV-2 and natural compounds

Predicted interaction between 14-deoxy-11,12-didehydroandrographolide with M^{pro} through -5.653 kcal/mole glide score displays conventional H bond formation occurs with Asn142 (bond length 2.387 Å) and Ser144 (bond length 3.432 Å) and Gln189 (bond length 3.216 Å) along with covalent bond formation at His41, Met49 (Fig. 4A, Table 1).

The in silico interactive study between andrograpanin and M^{pro} protease reveals binding affinities to Asn142 (bond length 2.437 Å), Cys145 (bond length 2.401Å) via H bonds together with His163 using alkyl, pi-alkyl interactions in autodock. Calculated glide score is -5.093 kcal/mole (Fig. 4B; Table 1).

The complexes obtained from both autodock and glide illustrate quinine interacts with the polar amino acids via a significant glide score of -5.002 kcal/mole. It shows the H bond with polar Cys145 (bond length 2.979 Å) carbon-hydrogen bond formations at Gln189. Additionally, hydrophobic interactions noted in His 41, Met 49 (Fig. 5A, Table 1).

Cinchonine shows a conventional H bond with Asn142 (bond length 2.345 Å), Cys145 (bond length 2.768 Å) and His164 (bond length 1.468 Å) with -5.585 kcal/mole glide score. Moreover, alkyl bond formation with nonpolar Met165. His41, Met 165 is also noticed (Fig. 5B; Table 1).

Molecular dynamics simulations

Root mean square deviation (RMSD) and Root Mean Square Fluctuation (RMSF) analysis

Root mean square deviation (RMSD) is one important aspect of Molecular Dynamic (MD) simulation as it determines the structural stability and conformational changes of protein-ligand docked complexes. The RMSD values in simulation trajectory signify lower RMSD is strong binding (Combrouse et al. 2013). The following equation expresses the RMSD.

$$RMSD_x = \sqrt{\frac{1}{N}\sum_{i=1}^{N} < (r_i'(t_x) - r_i(t_{ref}))^2 >}$$

where, N denotes the number of atoms in the atom selection; t_{ref} defines the reference time where t=0; r' represents the position of the selected atoms in the x frame after alignment with the reference frame. X frame noted at t_x time interval.

The crystallographic structure of four ligands namely, 14-deoxy-11,12-didehydroandrographolide, andrograpanin, quinine and cinchonine were selected for molecular simulation study towards M^{pro} of SARS-CoV and M^{pro} of SARS-CoV-2. In order to evaluate the binding stability of selected ligands into the binding sites of the two proteins, 50 ns MD was performed for each of the protein ligand complex. The RMSD values in simulation signify lower RMSD is strong binding. The RMSD of the Cα atoms of both the proteins i.e., M^{pro} (2GTB) of SARS-CoV and M^{pro} (6LU7) of SARS-CoV-2 in the protein-ligand complexes with andrograpanin and cinchonine (Figs. 6 and 7, blue traces) show structurally stable conformations throughout all of the simulations at equilibrium around the RMSD value of approximately 2.0–2.4 Å and 2.5 Å respectively with respect to the starting point of simulations. There is no significant difference observed in RMSD values of compounds 2 and compound 4 (Figs. 6 and 7, red traces) in complex with M^{pro} enzyme of SARS-CoV. The RMSD oscillates around less than 2.25 Å to 2.8 Å in a protein complex with andrpgrapanin, and cinchonine at the end of 50 ns. Comparatively, in the case of protease of SARS-CoV-2 andrograpanin show lesser RMSD values less than 2.4 Å which is an acceptable RMSD range (<4 Å).

RMSF calculations are advantageous for determining the local conformational changes through the protein chain in the docked complex by following the equation of simulation trajectory

$$RMSF_i = \sqrt{\frac{1}{T}\sum_{i=1}^{T} < (r_i'(t) - r_i(t_{ref}))^2 >}$$

where, T is expressed as trajectory time over the calculated RMSF, *tref* represents the reference time, *ri* stands for the position of residue *i*; *r'* is the position of atoms in residue *i* after alignment on the reference frame.

The local conformation changes in the main proteases of SARS-CoV and SARS-CoV-2 with all of the docked ligands were calculated in terms of deviations of the protein residues and atoms of the ligands in the docked complex. Interestingly, residues of the proteins in the obtained docked complexes of compounds 2 and 4 exhibit considerable RMSF values within 3-4 Å (Figs. S1 and S2). Besides, RMSF analysis of ligands molecules reveals there are no extreme fluctuations in the docked complexes noted in SARS-CoV and whereas only compound 2 show stability in case of SARS-CoV-2 (Figs. S3 and S4).

Post simulation protein-ligand interaction

Interactions of two proteases with four selected ligands were submitted to 50 ns MD simulation for a comparative pre and post-simulation analysis.

SARS-CoV

The diagrammatic illustration of post MD simulation shows that 14-deoxy-11,12-didehydroandrographolide interacted with M^{pro} of SARS-CoV with those residues which have been identified as active sites of the enzyme, specifically with Thr24, Thr24, Thr26, Leu27, His41, Cys44, Met49, Pro52, Tyr54, Asn142, Ser144, Cys145, Met165, Gln189, Thr190, and Gln192. The interactions are particularly comprised of hydrogen bonds and the formation of water bridges. However, a small number of hydrophobic interactions are noted (Figs. 8A, S5). Interestingly, Cys44, Met165, and Gln192 have interacted with ligands more than 50% of the total simulation time (Fig. S13A).

The post MD simulation diagram displays interactions of andrograpanin with M^{pro} of SARS-CoV involve Thr24, His41, Gly143, Met49, Phe140, Leu141, Asn142, Ser144, Cys145, His163, His164, Met165, Glu166, Gln189, Thr190 and Gln192 (Figs. 8B, S6). Gln143, Ser144, thr190 and Gln192 show 50% of the interactions involving water bridges and H bond formation of total simulation time (Fig. S13B).

The post-simulation analysis reveals quinine interacts with the protease of SARS-CoV involve hydrophobic interactions and water bridge formation with a wide range of residues of the active site (Thr25, Thr26, Leu27, His41, Cys44, Met49, Tyr111, Phe140, Leu141, Asn142, Ser144, Cys145, His163, His164, Met165, and Gln189) with lesser percentage due to its higher motility of the ligand molecule (Figs. 8C, S7). His41 shows >80% interaction of the total simulation time through hydrophobic bond formation (Fig. S13C).

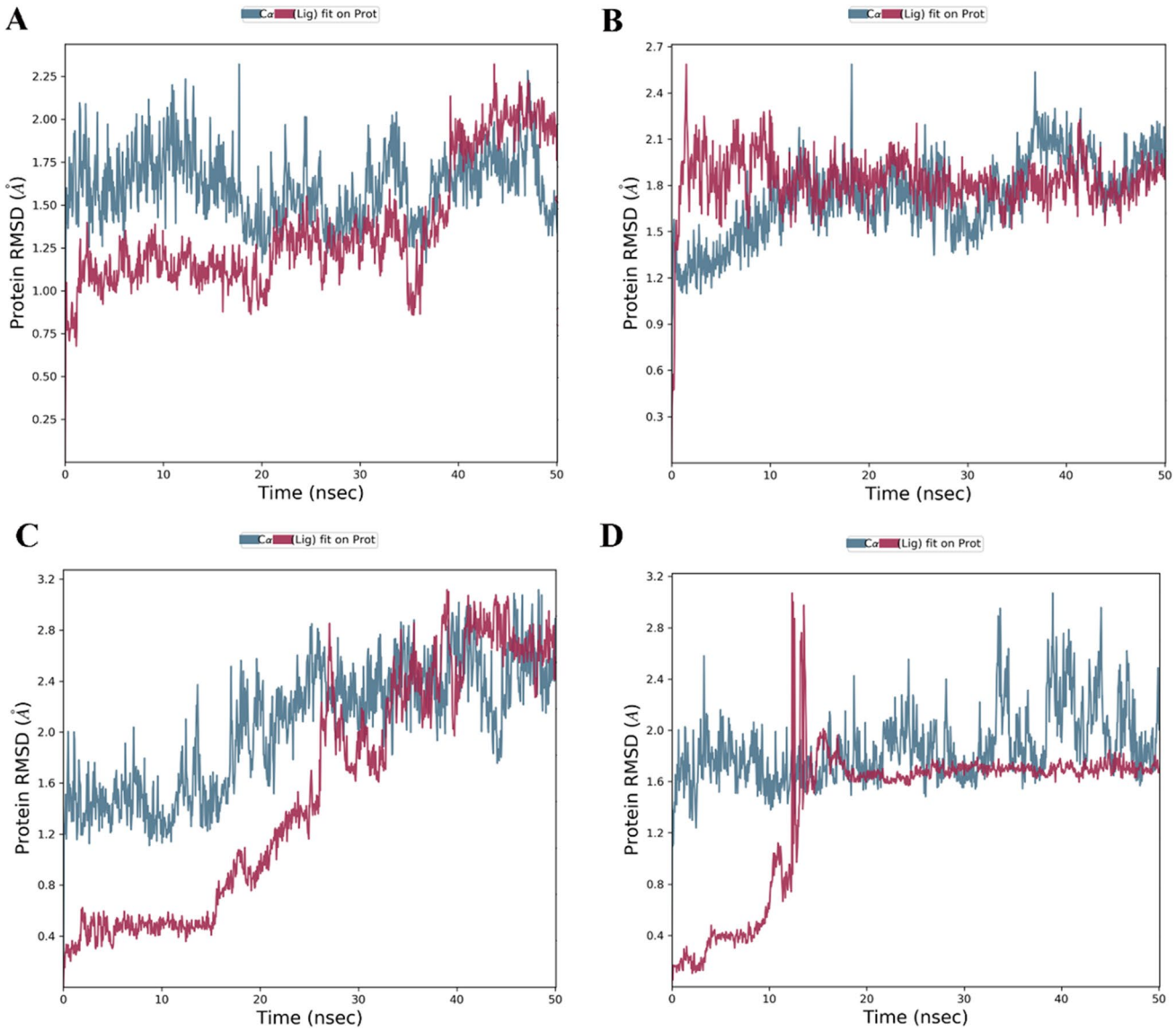

Fig. 6 RMSD values of backbonealpha carbon atoms of natural compounds (maroon curves) of and SARS-CoV M^{pro} (PDB ID 2GTB) and (bluecurves) of complexes during MD simulation, (**A**) 11, 12 deoxy-14didehydroandrographolide, (**B**), Andrograpanin, (**C**) Quinine, (**D**) Cinchonine withrespect to 50 ns simulation time

Also resembling quinine, cinchonine exhibits interactions with a comprehensive series of residues, including Glu14, Met17, Thr24, His41, Cys44, Met49, Phe140, Leu141, Asn142, Ser144, Cys145, His163, His164, Met165, Gln189, and Asp245 (Figs. 8D, S8). Notably, Val73 and Pro96 show 70% interactions of the total simulation time through hydrophobic bond formation (Fig. S13D).

SARS-CoV-2

Post-MD simulation reveals the main protease of SARS-CoV-2 displays interactions involves active site residue with 14-deoxy-11,12-didehydroandrographolide involve Thr25, Thr26, Leu27, His41, Val42, Met49, Tyr54, Leu141, Asn142, Cys145, His164, Met165, and Gln189 using hydrogen bond along with hydrophobic interactions and water bridges (Figs. 9A, S9). 80% of the bond formation takes place between the ligand and the Thr25 of total simulation time (Fig. S14A).

The post MD simulation demonstrates andrograpanin interacts with the main protease of SARS-CoV-2 at active sites involve Thr26, His41, Met49, Thr54, Leu141, Cys145, Asn142, Ser144, His163, His164, Met165, Gln189, and Thr190 by H bond, hydrophobic interactions, and water bridges (Figs. 9B, S10). Over 60% of interactions take place employing Met49, Met165, and Thr190 (Fig. S14B).

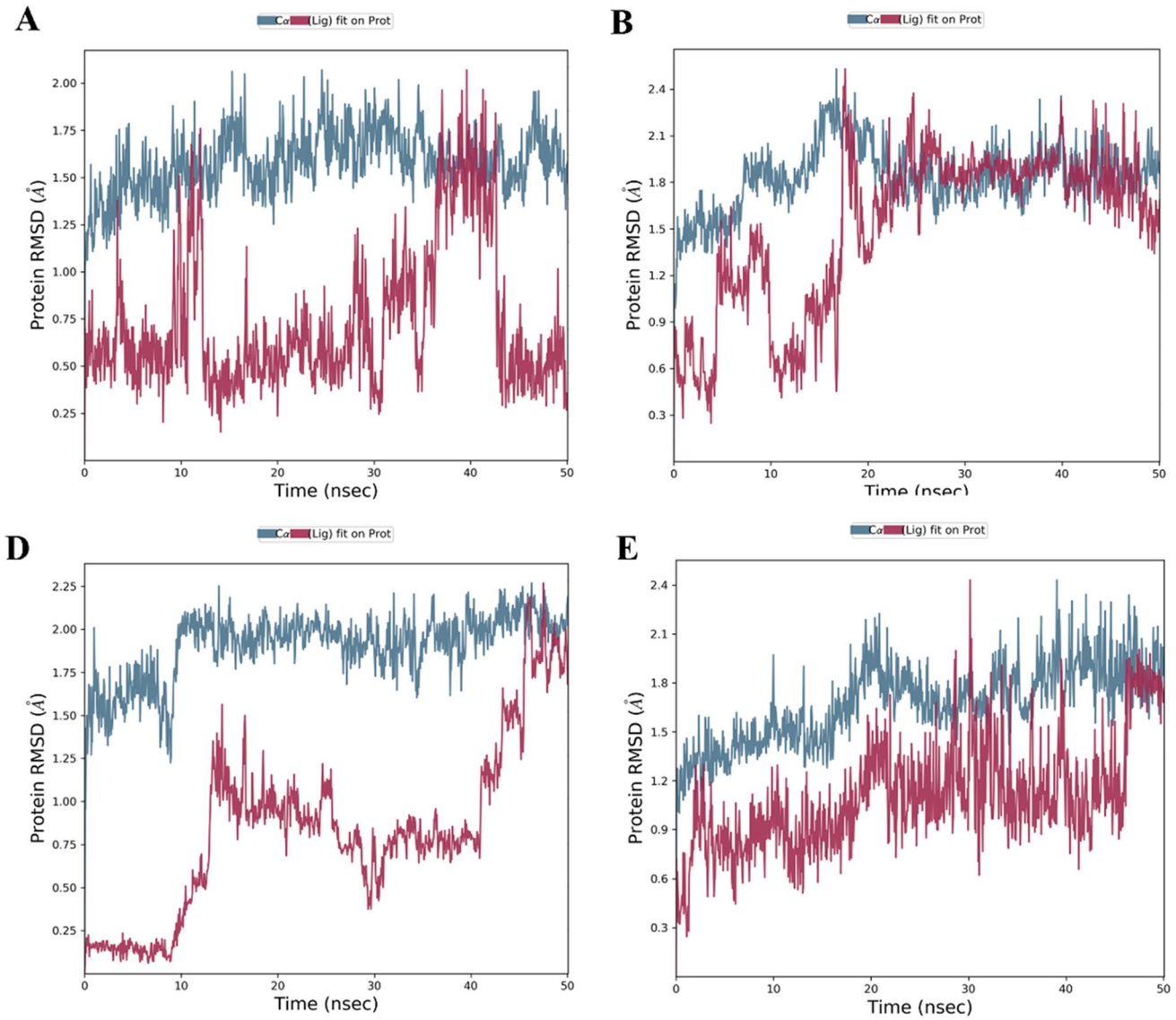

Fig. 7 RMSD values of backbonealpha carbon atoms of natural compounds (maroon curves) of and SARSCoV-2 M^{pro} (PDB ID 6LU7) and (blue curves) of complexes during MD simulation, (**A**) 11, 12deoxy-14 didehydroandrographolide, (**B**), Andrograpanin, (**C**) Quinine, (**D**)Cinchonine with respect to 50 ns simulation time

Quine displays molecular interaction in post MD simulation with active site residues of protein M^{pro} of SARS-CoV-2 at Leu27, His41, Cys44, Met49, Pro52, Tyr54, Cys145, His164, Met165, Glu166, Leu167, Pro168, Gln189, and Thr190, especially with H bond formation along with a little hydrophobic interaction (Figs. 9C, S11). Quinine interacts with Gln189 more than 90% of the total simulation time (Fig. S14C).

Besides, post-MD simulations unveil that cinchonine shows considerably rigid interactions with His41, Met49, Tyr54, Asn142, Ser144, Cys145, His163, His164, Met165, and Gln189 and Thr190 using hydrogen and hydrophobic bond formations (Figs. 9D, S12). Met165 exhibits >95% interaction with ligand present of the total simulation time (Fig. S14D).

Analysis of Molecular mechanics-generalized born surface area (MMGBSA)

A comparative analysis between 14-deoxy-11,12-didehydroandrographolide, andrographolide, quinine, and cinchonine with SARS-CoV or SARS-Cov-2 M^{pro} is illustrated in the MMGBSA study using binding energy, which is liberated during the process of bond formation amid protein and ligand. Lesser binding energy signifies the greater binding affinity of the ligands with target proteins (Genheden and

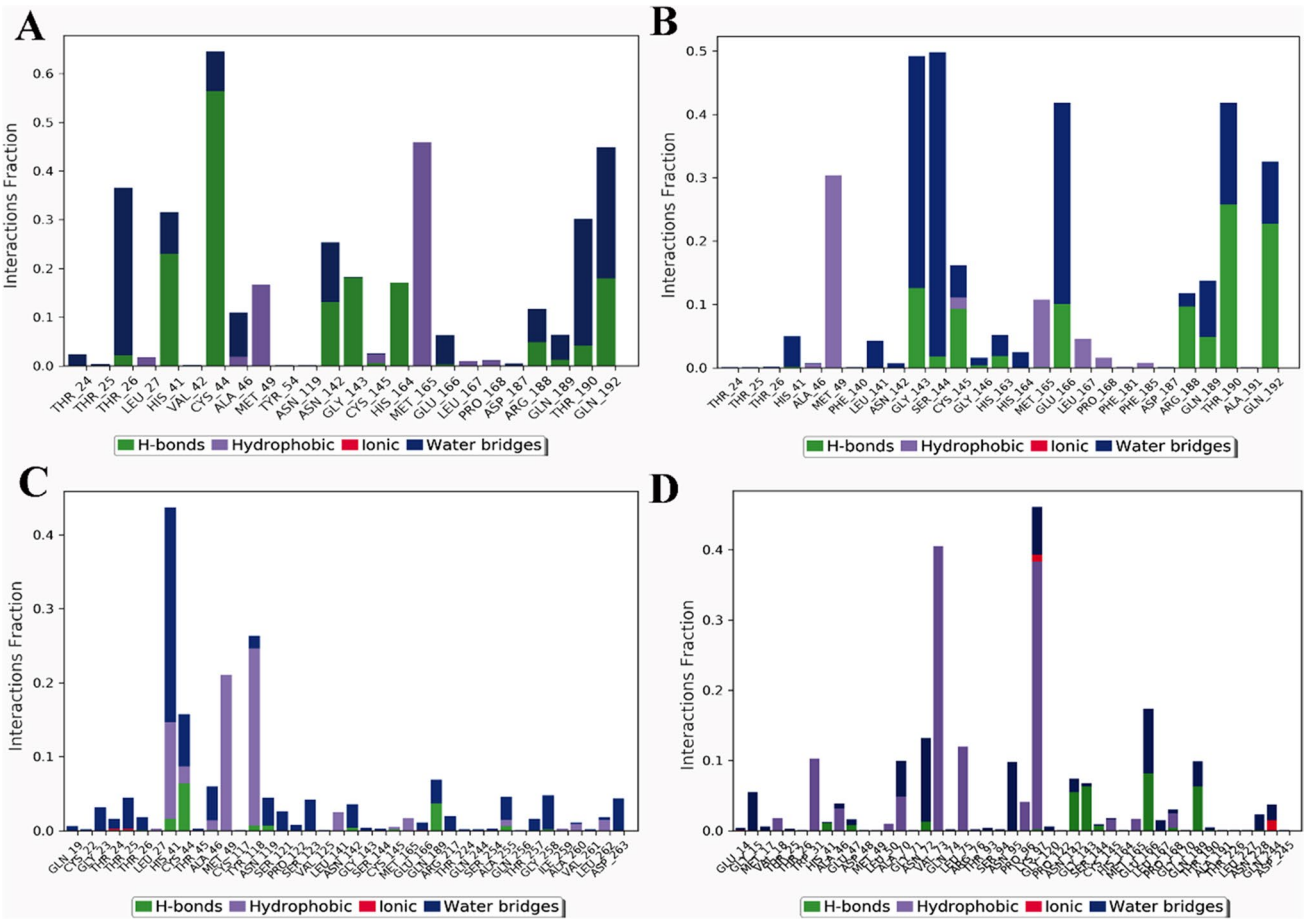

Fig. 8 Imageshowing protein-ligand contacts through MD simulations. The bar chart shows thepercentage and the type of interactions between SARS-CoV M^{pro} (PDB ID 2GTB) andnatural products; (**A**) 14-deoxy-11,12-didehydroandrographolide, (**B**) Andrograpanin, (**C**) Quinine, and (**D**)Cinchonine

Ryde 2015). A cumulative sum of the polar, electrostatic, van der Wall, and SASA energy is expressed as the final binding energy. The MMGBSA scores reveal that cinchonine has maximum negative scores at the time of interactions with the main protease of SARS-CoV, which signifies stronger affinities towards target protein (Table 3). Other calculated MMGBSA energies, specifically coulomb, covalent, H bond, solvation, vander Walls, are represented in Table 3.

Determination of half of the inhibitory concentration (IC50)

To understand the probable experimental anti-viral activities of the selected four ligands, half maximal value of inhibitory concentration (IC50) was predicted. The IC50 value is typically beneficial to measure a compound's efficacy to inhibit a given biological process by half partially (Burlingham and Widlanski 2003). The predicted IC50 values for 14-deoxy-11,12-didehydroandrographolide, andrograpanin, quinine, and cinchonine are 15.8 µM, 14.42 µM, 57.92 µM, and 168.08 µM for the main protease of SARS-CoV respectively. The predicted IC50 values for 14-deoxy-11,12-didehydroandrographolide, andrograpanin, quinine, and cinchonine are 107.32 µM, 456.72 µM, 636.1 µM, and 592.22 µM for M^{pro} of SARS-CoV-2, respectively.

Discussion

To become a fully mature virion, the viral proteins have gone through transcriptional and translational modifications (Fung and Liu 2018; Gale Jr et al. 2000). Therefore, the essential transcriptional proteins, such as viral proteases, can be considered potential targets for antiviral drug development. The main protease M^{pro} of SARS-CoV-2 has 96% sequence similarity with SARS-CoV (Chen et al. 2020). Therefore, the drug candidate, which shows attenuation M^{pro} activity of SARS-CoV, can be substantially effective against the M^{pro} activity of SARS-CoV-2. This M^{pro} is a cysteine peptidase in nature and regulates the replicase complex's formation through the massive processing of two

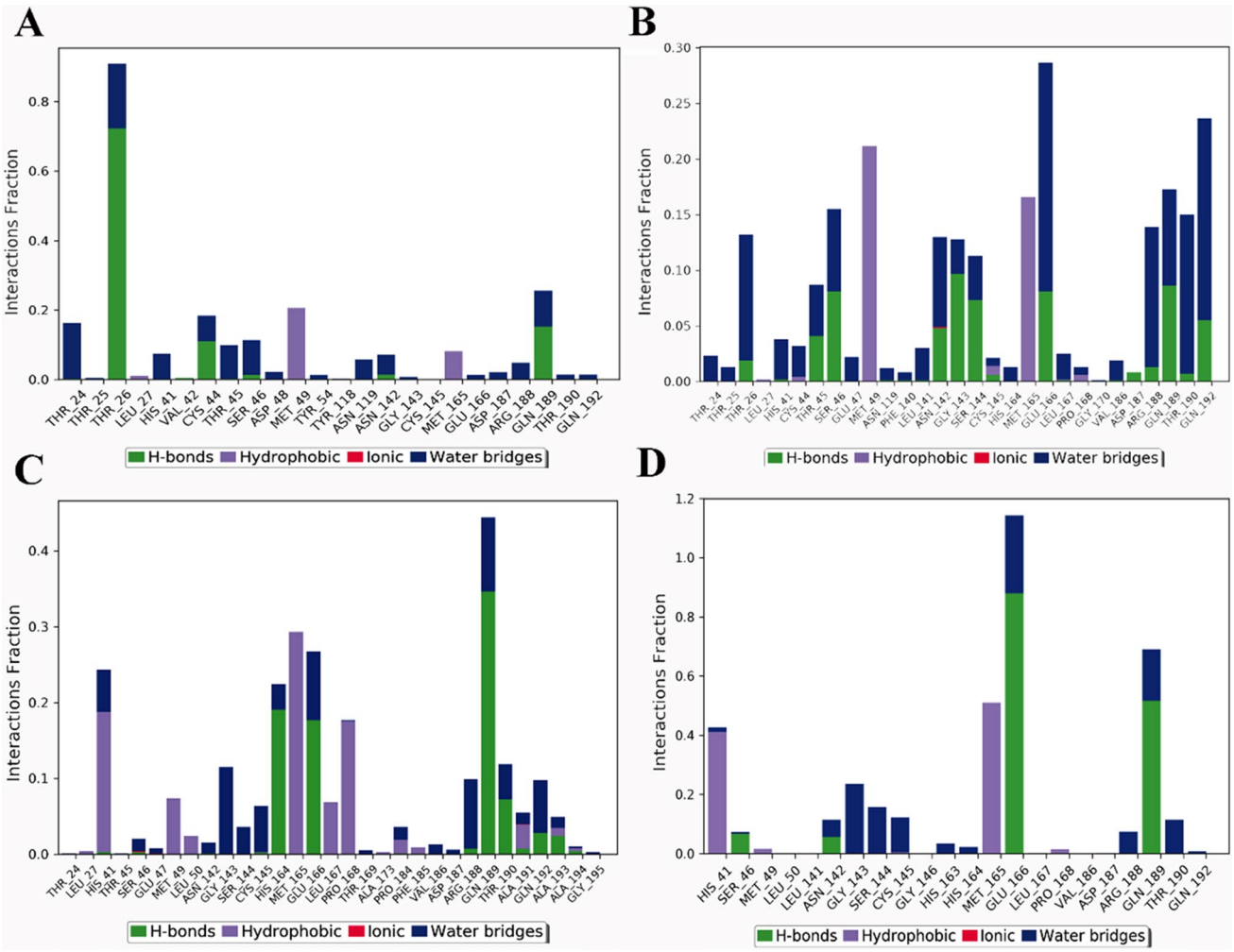

Fig. 9 Image showingprotein-ligand contacts through MD simulations. The bar chart shows thepercentage and the type of interactions between SARS-CoV-2 M^{pro} (PDB ID 6LU7) and natural products; (**A**) 14-deoxy-11,12- didehydroandrographolide, (**B**)Andrograpanin, (**C**) Quinine, and (**D**) Cinchonine

polyproteins. Two polyproteins are cleaved at 11 positions in the central and C-proximal regions by the M^{pro}, which allow the RNA polymerase and the helicase to initiate viral replication (Thiel et al. 2003). The main protease of SARS-CoV-2, also known as M^{pro} has a crucial role in processing the polyproteins that are translated directly from the viral RNA (Hilgenfeld 2014), along with viral replication and transcription (Jin et al. 2020).

Alkaloids, terpenoids, flavonoids, and polyphenols are present in the different parts of the plants; those are suitable to treat inflammation (Liu et al. 2008; Roy et al. 2010), fungal, bacterial, and viral infections like HSV, HIV, influenza virus, etc. (Majumdar and Roy 2019). Different parts of a plant, along with extracts of some eminent medicinal plants, namely *Andrographis paniculata*, *Cinchona officinalis*, are used as anti-inflammatory (Liu et al. 2008; Roy et al. 2010, 2011), anti-parasitic (Achan et al. 2011), anti-fungal (Solary et al. 2000), anti-bacterial and anti-viral (J.-X. Chen et al. 2009; Niranjan Reddy et al. 2005) medications due to the presence of active biomolecules as their secondary metabolites. One more diterpenoid, andrograpanin (Fig. 1), isolated from *Andrographis paniculata* is a hydrolyzed form of neoandrographolide (Liu et al. 2008) and is majorly used to treat inflammation, fever, and diarrhea, etc. (Ji et al. 2005). Another well-known medicinal plant, *Cinchona officinalis* contains some naturally occurring alkaloids like quinine, quinidine, cinchonine, and cinchonidine (Fig. 1) present in the bark of the tree (Bharadwaj et al. 2018). On the structural aspect, they all possess a commonly substituted quinoline moiety and a substituted quinuclidine ring. One carbon center acts as a linker between these two units. Quinine is well known for its novel anti-malarial effects (Achan et al. 2011). It also has the potential to treat some serious viral infections like HSV (Baroni et al. 2007). Alike quinine,

Table 3 MMGBSA binding score of 14-deoxy-11,12-didehydroandrographolide, andrograpanin, quinine and cinchonine against main proteases of SARS-CoV and SARS-CoV-2

Protein (PDB ID)	Compound (PubChem ID)	MMGBSA dG Bind	MMGBSA dG Bind Coulomb	MMGBSA dG Bind Covalent	MMGBSA dG Bind Hbond	MMGBSA dG Bind Solv GB	MMGBSA dG Bind vdW
M^{pro} (2GTB)	14-deoxy-11,12-didehydroandrographolide (PubChem ID: 5708351)	-50.75	-9.52	7.36	-0.52	17.74	-25.761
	Andrograpanin (PubChem ID: 11666871)	-46.07	-9.57	3.35	-0.90	17.80	-31.232
	Quinine (Pubchem ID: 3034034)	-51.09	-24.61	1.93	-0.44	32.85	-29.349
	Cinchonine (Pubchem ID: 90454)	-52.58	-20.49	3.70	-0.25	31.69	-34.587
M^{pro} (6LU7)	14-deoxy-11,12-didehydroandrographolide (PubChem ID: 5708351)	-52.09	-0.87	2.08	-0.30	16.74	-30.262
	Andrograpanin (PubChem ID: 11666871)	-55.18	-6.04	6.22	-0.47	10.69	-33.448
	Quinine (Pubchem ID: 3034034)	-60.39	-26.63	3.57	-0.29	33.39	-36.951
	Cinchonine (Pubchem ID: 90454)	-61.89	-25.06	1.73	-0.25	27.61	-32.325

cinchonine, has also been implemented as a leading anti-malarial drug (Achan et al. 2011).

In the present study, molecular docking and MD simulation were performed to get an idea about the mode of action of some selected natural products with medicinal values like 14-deoxy-11,12-didehydroandrographolide, andrograpanin, quinine, cinchonine against the main protease of SARS-CoV and SARS-CoV-2. After docking analysis, the protein-ligand complex for each of the four compounds has been subjected to 50ns Molecular Dynamics simulation studies. The protein-ligand complex of SARS-CoV and SARS-Cov-2 was compared for pre and post-MD simulation to validate binding and other critical parameters. The four compounds were screened against the main proteinase of SARS-CoV and SARS-CoV-2. Three parameters were considered involving (1) root mean square deviation (RMSD) for structural stability, (2) root mean square fluctuation (RMSF) for measuring local fluctuations, and (3) mapping of protein-ligand contacts for active site binding affinities.

Structure-based sequence alignment studies of the main proteases of SARS-CoV confirmed that M^{pro} specially cleaves at a consensus sequence for the P4 to P1 residues (Anand et al. 2003). The active site residues of P1 space reported to include His41, Phe140, Cys145, Tyr 161, His163, Glu166, His172 (Citarella et al. 2021; Lee et al. 2007) Andrograpanin (Pubchem ID: 11,666,871) from *A. paniculata* displays non-covalent interactions with main protease enzymes. Similar active site interactions with significant docking energies and MMGBSA scores and MD simulations reveal that andrograpnin (Fig. 1) also interacts with the same cavity compared with the reported ligands in the crustal structure of the proteins (Lee et al. 2007). Under the purview of the chemical structure of andrograpanin, it possesses a central lactone moiety with pi-electron in its 14th position, which is favorable for alkyl and pi-alkyl bond formation by H bond donor activity (5 scores according to calculated ADMET) with 4 rotatable bonds. The >C=O group (Fig. 1), acting as hydrogen bond acceptor (9 scores according to calculated ADMET, data has not shown) with 10 rotatable bonds, whereas –NH or the –COOH terminal of the amino acids of the M^{pro} play the role of H-bond donor. Post simulation analysis reveals this compound exhibits H bond formation with an acceptable range of protein-ligand RMSD (< 4 Å) and RMSF with stable contact active site residues of target proteins after 50ns simulation. Further, post-simulation conformational stability of protein-ligand complexes for both SARS-CoV and SARS-CoV-2 confirms andrograpanin has high binding affinities towards target proteins' active sites. Moreover, after analyzing the pre and post-simulation data reveal andrograpanin competitively inhibits the main protease of SARS-CoV-2 (Fig. S16B) compared with the reported N3 inhibitor (Jin et al. 2020). Andrograpanin was previously reported to have potential inhibitory activities against HIV and 3CLpro of SARS-CoV-2 (Niranjan Reddy et al. 2005; Wu et al. 2020). On the other hand, cinchonine (Pubchem ID: 90,454) exhibits stable binding interactions with SARS-CoV M^{pro} (Fig. S15D) after evaluating two major docking platforms and three parameters of MD simulation trajectories with 3 rotatable bonds. Pi-electron cloud of the aromatic ring in cinchonine interacts with the pi-electron of the methyl group in methionine resulted in the formation of an alkyl bond in-between ligand and amino

acid residue. Additionally, H bond is formed between protein and ligand utilizing of >C=O group of cinchonine (2-20 score according to calculated ADMET) and –NH terminal of asparagine in target protease. The predicted IC50 values against SARS-CoV (168.08 µM) which is nontoxic to the humans (Barennes et al. 1996).

Conclusions

At present, there are no approved drugs against COVID-19; the disease has emerged as the highest threat to the global human population. Under this circumstance, it's enormously required to develop novel medications to fight against SARS-CoV-2. This study aims to evaluate four bioactive molecules from two medicinal plants that may act as inhibitors of the COVID-19 viral maturation cycle. The *in-silico* studies suggest that among four compounds, andrograpanin can be considered as the potent inhibitor against SARS-CoV-2 M^{Pro}. Additionally, the RMSD trajectories exhibited that the selected complex is stable and comparable to previously reported structures. MD simulation revealed that andrograpanin interacts with strong binding energies in the active site of SARS-CoV-2M^{pro}. Furthermore, the predicted IC50 value and ADMET score specify it is nontoxic and devoid of any tumorigenic, mutagenic, or irritant properties. Hence, andrograpanin could be explored through *in vitro* and *in vivo* experiments as an impending attenuator of the main protease of SARS-CoV-2 in the near future for antiviral drug development against COVID-19.

Supplementary Information The online version contains supplementary material available at https://doi.org/10.1007/s11756-022-01012-y.

Acknowledgements MM is thankful to the National Institute of Technology-Agartala for providing the Ph.D. fellowship.

Author contributions MM performed the experiments, analyzed the results, and wrote the manuscript. VS performed a few experiments. TKM analyzed the results. DNR designed the experiments, analyzed the results, and helped to write the manuscript.

Data availability The raw data files are available with the corresponding author.

Code availability The softwares used in the study are mentioned in the material and methods.

Declarations

Conflict of interest There is no conflict of interest to proclaim.

References

Achan J, Talisuna AO, Erhart A, Yeka A, Tibenderana JK, Baliraine FN, D'Alessandro U (2011) Quinine, an old anti-malarial drug in a modern world: role in the treatment of malaria. Malar J 10(1):1–12. https://doi.org/10.1186/1475-2875-10-144

Anand K, Ziebuhr J, Wadhwani P, Mesters JR, Hilgenfeld R (2003) Coronavirus main proteinase (3CLpro) structure: basis for design of anti-SARS drugs. Science 300(5626):1763–1767. https://doi.org/10.1126/science.1085658

Astuti I (2020) Severe Acute Respiratory Syndrome Coronavirus 2 (SARS-CoV-2): An overview of viral structure and host response. Diabetes Metab Syndr 14(4):407–412. https://doi.org/10.1016/j.dsx.2020.04.020

Barennes H, Pussard E, Sani AM, Clavier F, Henzel D, Kahiatani F, Verdier F (1996) Intrarectal Quinimax®(a combination of cinchona alkaloids) administered at 3 different dosages to children with Plasmodium falciparum malaria in Niger. Clin Drug Investig 11(3):154–158. https://doi.org/10.2165/00044011-199611030-00005

Baroni A, Paoletti I, Ruocco E, Ayala F, Corrado F, Wolf R, Donnarumma G (2007) Antiviral effects of quinine sulfate on HSV-1 HaCat cells infected: analysis of the molecular mechanisms involved. J Dermatol Sci 47(3):253–255. https://doi.org/10.1016/j.jdermsci.2007.05.009

Bharadwaj KC, Gupta T, Singh RM (2018) Alkaloid group of Cinchona officinalis: structural, synthetic, and medicinal aspects Synthesis of Medicinal Agents from Plants. Elsevier, Amsterdam, pp 205–227. https://doi.org/10.1016/B978-0-08-102071-5.00009-X

Bowers KJ, Chow DE, Xu H, Dror RO, Eastwood MP, Gregersen BA, Sacerdoti FD (2006) Scalable algorithms for molecular dynamics simulations on commodity clusters. Paper presented at the SC'06: Proceedings of the 2006 ACM/IEEE Conference on Supercomputing

Burlingham BT, Widlanski TS (2003) An intuitive look at the relationship of Ki and IC50: a more general use for the Dixon plot. J Chem Educ 80(2):214. https://doi.org/10.1021/ed080p214

Chen J-X, Xue H-J, Ye W-C, Fang B-H, Liu Y-H, Yuan S-H, Wang Y-Q (2009) Activity of andrographolide and its derivatives against influenza virus in vivo and in vitro. Biol Pharm Bull 32(8):1385–1391. https://doi.org/10.1248/bpb.32.1385

Chen YW, Yiu C-PB, Wong K-Y (2020) Prediction of the SARS-CoV-2 (2019-nCoV) 3 C-like protease (3CL pro) structure: virtual screening reveals velpatasvir, ledipasvir, and other drug repurposing candidates. F1000Research 9. https://doi.org/10.12688/f1000research.22457.2

Citarella A, Scala A, Piperno A, Micale N (2021) SARS-CoV-2 Mpro: A potential target for peptidomimetics and small-molecule inhibitors. Biomolecules 11(4):607. https://doi.org/10.3390/biom11040607

Combrouse T, Sadovskaya I, Faille C, Kol O, Guerardel Y, Midelet-Bourdin G (2013) Quantification of the extracellular matrix of the L isteria monocytogenes biofilms of different phylogenic lineages with optimization of culture conditions. J Appl Microbiol 114(4):1120–1131. https://doi.org/10.1111/jam.12127

Cragg GM, Newman DJ (2013) Natural products: a continuing source of novel drug leads. Biochim Biophys Acta (BBA)-Gen Subj 1830(6):3670–3695. https://doi.org/10.1016/j.bbagen.2013.02.008

Dubey A, Dotolo S, Ramteke PW, Facchiano A, Marabotti A (2019) Searching for chymase inhibitors among chamomile compounds

using a computational-based approach. Biomolecules 9(1):5. https://doi.org/10.3390/biom9010005

Dubey A, Marabotti A, Ramteke PW, Facchiano A (2016) Interaction of human chymase with ginkgolides, terpene trilactones of Ginkgo biloba investigated by molecular docking simulations. Biochem Biophys Res Commun 473(2):449–454. https://doi.org/10.1016/j.bbrc.2016.03.028

Fehr AR, Perlman S (2015) Coronaviruses: an overview of their replication and pathogenesis. Methods Mol Biol 1282:1–23. https://doi.org/10.1007/978-1-4939-2438-7_1

Fung TS, Liu DX (2018) Post-translational modifications of coronavirus proteins: roles and function. Future Virol 13(6):405–430. https://doi.org/10.2217/fvl-2018-0008

Gale Jr M, Tan S-L, Katze MG (2000) Translational control of viral gene expression in eukaryotes. Microbiol Mol Biol Rev 64(2):239–280. https://doi.org/10.1128/MMBR.64.2.239-280.2000

Gasteiger J, Marsili M (1980) Iterative partial equalization of orbital electronegativity—a rapid access to atomic charges. Tetrahedron 36(22):3219–3228. https://doi.org/10.1016/0040-4020(80)80168-2

Genheden S, Ryde U (2015) The MM/PBSA and MM/GBSA methods to estimate ligand-binding affinities. Expert Opin Drug Discov 10(5):449–461. https://doi.org/10.1517/17460441.2015.1032936

Hilgenfeld R (2014) From SARS to MERS: crystallographic studies on coronaviral proteases enable antiviral drug design. FEBS J 281(18):4085–4096. https://doi.org/10.1111/febs.12936

Ji LL, Wang Z, Dong F, Zhang WB, Wang ZT (2005) Andrograpanin, a compound isolated from anti-Inflammatory traditional Chinese medicine Andrographis paniculata, enhances chemokine SDF-1α-induced leukocytes chemotaxis. J Cell Biochem 95(5):970–978. https://doi.org/10.1002/jcb.20464

Jin Z, Du X, Xu Y, Deng Y, Liu M, Zhao Y, Peng C (2020) Structure of M pro from SARS-CoV-2 and discovery of its inhibitors. Nature 582(7811):289–293. https://doi.org/10.1038/s41586-020-2223-y

Kaur J, Sundar S, Singh N (2010) Molecular docking, structure–activity relationship and biological evaluation of the anticancer drug monastrol as a pteridine reductase inhibitor in a clinical isolate of Leishmania donovani. J Antimicrob Chemother 65(8):1742–1748. https://doi.org/10.1093/jac/dkq189

Lee T-W, Cherney MM, Liu J, James KE, Powers JC, Eltis LD, James MN (2007) Crystal structures reveal an induced-fit binding of a substrate-like Aza-peptide epoxide to SARS coronavirus main peptidase. J Mol Biol 366(3):916–932. https://doi.org/10.1016/j.jmb.2006.11.078

Lei J, Kusov Y, Hilgenfeld R (2018) Nsp3 of coronaviruses: Structures and functions of a large multi-domain protein. Antiviral Res 149:58–74. https://doi.org/10.1016/j.antiviral.2017.11.001

Li H, Qin H, Wang W, Li G, Wu C, Song J (2006) Effect of andrographolide on QS regulating virulence factors production in Pseudomonas aeruginosa. Zhongguo Zhong yao za zhi= Zhongguo zhongyao zazhi= China J Chin Mater Med 31(12):1015-1017

Liu J, Wang Z-T, Ge B-X (2008) Andrograpanin, isolated from Andrographis paniculata, exhibits anti-inflammatory property in lipopolysaccharide-induced macrophage cells through down-regulating the p38 MAPKs signaling pathways. Int Immunopharmacol 8(7):951–958. https://doi.org/10.1016/j.intimp.2007.12.014

Majumdar M, Biswas SC, Choudhury R, Upadhyay P, Adhikary A, Roy DN, Misra TK (2019) Synthesis of gold nanoparticles using citrus Macroptera fruit extract: anti-biofilm and anticancer activity. ChemistrySelect 4(19):5714–5723. https://doi.org/10.1002/slct.201804021

Majumdar M, Dubey A, Goswami R, Misra TK, Roy DN (2020a) In vitro and in silico studies on the structural and biochemical insight of anti-biofilm activity of andrograpanin from Andrographis paniculata against Pseudomonas aeruginosa. World J Microbiol Biotechnol 36(10):1–18. https://doi.org/10.1007/s11274-020-02919-x

Majumdar M, Khan SA, Biswas SC, Roy DN, Panja AS, Misra TK (2020b) In vitro and in silico investigation of anti-biofilm activity of Citrus macroptera fruit extract mediated silver nanoparticles. J Mol Liq 302:112586. https://doi.org/10.1016/j.molliq.2020.112586

Majumdar M, Khan SA, Nandi NB, Roy S, Panja AS, Roy DN, Misra TK (2020c) Green synthesis of iron nanoparticles for investigation of biofilm inhibition property. ChemistrySelect 5(43):13575–13583. https://doi.org/10.1002/slct.202003033

Majumdar M, Misra TK, Roy DN (2020d) In vitro anti-biofilm activity of 14-deoxy-11, 12-didehydroandrographolide from Andrographis paniculata against Pseudomonas aeruginosa. Braz J Microbiol 51(1):15–27. https://doi.org/10.1007/s42770-019-00169-0

Majumdar M, Shivalkar S, Pal A, Verma ML, Sahoo AK, Roy DN (2020e) Nanotechnology for enhanced bioactivity of bioactive compounds. Biotechnological Production of Bioactive Compounds. Elsevier, Amsterdam, pp 433–466

Majumdar M, Roy DN (2019) Terpenoids: the biological key molecules. Terpenoids Against Human Diseases. CRC Press, Boca Raton, pp 39–60

McIntosh K, Hirsch MS, Bloom A (2021) COVID-19: Epidemiology, virology, and prevention. UpToDate. Available online: https://www.uptodate.com/contents/covid-19-epidemiology-virology-andprevention. Accessed 18 March 2021

Morris GM, Huey R, Lindstrom W, Sanner MF, Belew RK, Goodsell DS, Olson AJ (2009) AutoDock4 and AutoDockTools4: Automated docking with selective receptor flexibility. J Comput Chem 30(16):2785–2791. https://doi.org/10.1002/jcc.21256

Niranjan Reddy V, Malla Reddy S, Ravikanth V, Krishnaiah P, Venkateshwar Goud T, Rao T, Venkateswarlu Y (2005) A new bisandrographolide ether from Andrographis paniculata nees and evaluation of anti-HIV activity. Nat Prod Res 19(3):223–230. https://doi.org/10.1080/14786410410001709197

Olsson MH, Søndergaard CR, Rostkowski M, Jensen JH (2011) PROPKA3: consistent treatment of internal and surface residues in empirical p K a predictions. J Chem Theory Comput 7(2):525–537. https://doi.org/10.1021/ct100578z

Organization WH (2003) Summary of probable SARS cases with onset of illness from 1 November 2002 to 31 July 2003. http://www.who.int/csr/sars/country/table2004_04_21/en/index.html, https://www.ijbs.com/v16p1678.htm

Rao CMMP, Yejella RP, Rehman RSA, Basha SH (2015) Molecular docking based screening of novel designed chalcone series of compounds for their anti-cancer activity targeting EGFR kinase domain. Bioinformation 11(7):322. https://doi.org/10.6026/97320630011322

Roy D, Mandal S, Sen G, Mukhopadhyay S, Biswas T (2010) 14-Deoxyandrographolide desensitizes hepatocytes to tumour necrosis factor-alpha-induced apoptosis through calcium-dependent tumour necrosis factor receptor superfamily member 1A release via the NO/cGMP pathway. Br J Pharmacol 160(7):1823–1843. https://doi.org/10.1111/j.1476-5381.2010.00836.x

Roy DN, Sen G, Chowdhury KD, Biswas T (2011) Combination therapy with andrographolide and d-penicillamine enhanced therapeutic advantage over monotherapy with d-penicillamine in attenuating fibrogenic response and cell death in the periportal zone of liver in rats during copper toxicosis. Toxicol Appl Pharmcol 250(1):54–68. https://doi.org/10.1016/j.taap.2010.09.027

Sahin A, Erdogan A, Agaoglu P, Dineri Y, Cakirci A, Senel M (2019) novel coronavirus (COVID-19) outbreak: A review of the current literature. EJMO 2020; 4: 1-7. Publisher Full Text. https://doi.org/10.14744/ejmo.2020.12220

Shelley JC, Cholleti A, Frye LL, Greenwood JR, Timlin MR, Uchimaya M (2007) Epik: a software program for pK a prediction and protonation state generation for drug-like molecules. J Comput Aided Mol Des 21(12):681–691. https://doi.org/10.1007/s10822-007-9133-z

Solary E, Mannone L, Moreau D, Caillot D, Casasnovas R, Guy H, Fenaux P (2000) Phase I study of cinchonine, a multidrug resistance reversing agent, combined with the CHVP regimen in relapsed and refractory lymphoproliferative syndromes. Leukemia 14(12):2085–2094. https://doi.org/10.1038/sj.leu.2401945

Sturman LS, Holmes KV (1983) The molecular biology of coronaviruses. Adv Virus Res 28:35–112. https://doi.org/10.1016/0168-1702(86)90074-2

Talactac MR, Chowdhury MY, Park M-E, Weeratunga P, Kim T-H, Cho W-K, Lee J-S (2015) Antiviral effects of novel herbal medicine KIOM-C, on diverse viruses. PLoS ONE 10(5):e0125357. https://doi.org/10.1371/journal.pone.0125357

Thiel V, Herold J, Schelle B, Siddell SG (2001) Viral replicase gene products suffice for coronavirus discontinuous transcription. J Virol 75(14):6676–6681. https://doi.org/10.1128/JVI.75.14.6676-6681.2001

Thiel V, Ivanov KA, Putics A, Hertzig T, Schelle B, Bayer S, Doerr HW (2003) Mechanisms and enzymes involved in SARS coronavirus genome expression. J Gen Virol 84(9):2305–2315. https://doi.org/10.1099/vir.0.19424-0

Wei M, Wynn R, Hollis G, Liao B, Margulis A, Reid BG, Rupar M (2007) High-throughput determination of mode of inhibition in lead identification and optimization. J BioMol Screen 12(2):220–228. https://doi.org/10.1177/1087057106296679

Wu C, Liu Y, Yang Y, Zhang P, Zhong W, Wang Y, Li X (2020) Analysis of therapeutic targets for SARS-CoV-2 and discovery of potential drugs by computational methods. Acta Pharm Sin B 10(5):766–788. https://doi.org/10.1016/j.apsb.2020.02.008

Xia B, Kang X (2011) Activation and maturation of SARS-CoV main protease. Protein Cell 2(4):282–290. https://doi.org/10.1007/s13238-011-1034-1

Xue X, Yu H, Yang H, Xue F, Wu Z, Shen W, Zhao Q (2008) Structures of two coronavirus main proteases: implications for substrate binding and antiviral drug design. J Virol 82(5):2515–2527. https://doi.org/10.1128/JVI.02114-07

Zheng J (2020) SARS-CoV-2: an emerging coronavirus that causes a global threat. Int J Biol Sci 16(10):1678. https://www.ncbi.nlm.nih.gov/pmc/articles/PMC7098030/

Zhou P, Liu Z, Chen Y, Xiao Y, Huang X, Fan X-G (2020a) Bacterial and fungal infections in COVID-19 patients: a matter of concern. Infect Control Hosp Epidemiol 41(9):1124–1125. https://doi.org/10.1017/ice.2020.156

Zhou P, Yang X-L, Wang X-G, Hu B, Zhang L, Zhang W, Huang C-L (2020b) A pneumonia outbreak associated with a new coronavirus of probable bat origin. Nature 579(7798):270–273. https://doi.org/10.1038/s41586-020-2012-7